Dalton Transactions

ROYAL SOCIETY OF CHEMISTRY

PAPER

View Article Online
View Journal | View Issue

Cite this: *Dalton Trans.*, 2023, **52**, 10437

On the importance of equatorial metal-centered excited states in the photophysics of cyclometallated Ir(III) complexes†

Iván Soriano-Díaz, Enrique Ortí * and Angelo Giussani *

In the present contribution, the following three cyclometallated Ir(III) complexes were theoretically investigated using density functional theory calculations to explain their different photophysical properties: [Ir(ppy)$_2$(bpy)]$^+$, where Hppy is 2-phenylpyridine and bpy is 2,2′-bipyridine, [Ir(ppy)$_2$(pbpy)]$^+$, where pbpy is 6-phenyl-2,2′-bipyridine, and [Ir(ppy)$_2$(dpbpy)]$^+$, where dpbpy is 6,6′-diphenyl-2,2′-bipyridine. Despite sharing the same molecular skeleton, with the only difference being the addition of one or two phenyl groups attached to the ancillary bpy ligand, the complexes show different emission quantum yields in CH_2Cl_2 solution (0.196, 0.049 and 0.036, respectively). Such a behavior was previously justified as a consequence of a different ability to non-radiatively decay through an axial metal-centered (MC) triplet state. In the present contribution, a new non-radiative decay path has been characterized to be mediated by the so-called equatorial MC states, in which an Ir–N_{bpy} bond is elongated instead of an Ir–N_{ppy} bond as observed in the axial MC states. The decay path involving the equatorial MC states is more favorable than that associated with the axial MC states, and the different ability to decay through the former better explains the photoemission properties exhibited by the three complexes.

Received 11th May 2023,
Accepted 26th June 2023

DOI: 10.1039/d3dt01404e

rsc.li/dalton

Introduction

Ionic transition-metal complexes (iTMCs) have been studied in recent years in relation to their use in light-emitting electrochemical cells (LECs).[1,2] In contrast to organic light-emitting diodes (OLEDs), LECs have a low production cost due to their simpler structure, which does not require a strict encapsulation.[3] The most commonly employed iTMCs for LECs are based on Ru(II) or Ir(III) centers. In general terms, the former, a second-row transition metal, presents lower emission quantum yields and efficiencies than a third-row transition metal such as Ir. These differences are explained by the lower ligand-field splitting energies of Ru(II) complexes, which facilitate the population of the metal-centered (MC) excited triplet states.[4] A high emission quantum yield is essential to obtain a good performance of the final LEC device. In addition to their use in LECs, Ir complexes also exhibit important applications in areas such as photocatalysis,[5] biological imaging,[6] luminescence sensitizers[7,8] and chemosensors.[9–11]

Among Ir complexes for electroluminescence applications, the most studied are the cyclometallated complexes based on the general formula [Ir(C^N)$_2$(N^N)]$^+$, the Ir[(ppy)$_2$(bpy)]$^+$ complex, where Hppy is 2-phenylpyridine and bpy is 2,2′-bipyridine, being the archetype reference of such a family. The photophysical properties of Ir[(ppy)$_2$(bpy)]$^+$ can be easily modified by the introduction of electronically active substituents. For example, the addition of fluoro and *tert*-butyl groups giving rise to the [Ir(diFppy)$_2$(dtb-bpy)]$^+$ complex, where diFHppy is 2-(2,4-difluorophenyl)pyridine and dtb-bpy is 4,4′-di-*tert*-butyl-2,2′-bipyridine, determines a significant increase of the emission quantum yield with respect to Ir[(ppy)$_2$(bpy)]$^+$ (from 0.196 to 0.71, respectively).[12] On the other hand, the addition of phenyl groups on the bpy ancillary ligand has the opposite effect. In fact, complexes [Ir(ppy)$_2$(pbpy)]$^+$ and [Ir(ppy)$_2$(dpbpy)]$^+$, where pbpy represents 6-phenyl-2,2′-bipyridine and dpbpy is 6,6′-diphenyl-2,2′-bipyridine, display significantly lower emission quantum yields of 0.049 and 0.036, respectively.[13]

It is generally accepted that, upon excitation, a common non-radiative decay path for iTMCs goes through the population of the triplet metal-centered states (^{3}MC).[14–17] In particular, for the family of [Ir(C^N)$_2$(N^N)]$^+$ complexes, such a state is associated with the so-called axial ^{3}MC, hereafter $^3MC_{ax}$, which leads to a strong geometrical distortion resulting from the elongation of the Ir–N_{C^N} bonds due to the occupation of the Ir e_g* molecular orbital (MO). Such a deformation determines a drastic reduction of the energy gap with the

Instituto de Ciencia Molecular, Universidad de Valencia, Catedrático José Beltrán 2, 46980 Paterna, Spain. E-mail: angelo.giussani@uv.es, enrique.orti@uv.es

† Electronic supplementary information (ESI) available. See DOI: https://doi.org/10.1039/d3dt01404e

ground state (S_0) at the corresponding $^3MC_{ax}$ minimum and the presence of a nearby T_1/S_0 singlet–triplet crossing (STC) region, leading the system back to the ground state in a non-radiative way.[12] Additionally, in other complexes where one pyridine ring of the ancillary ligand is substituted by a five-membered ring, another MC state (the so-called equatorial ^3MC, hereafter $^3MC_{eq}$), characterized by the elongation of the Ir–N_{N^N} bond of this ring and its rotation around the interring bond, has been localized. Consequently, in the $^3MC_{ax}$ state, the Ir atom still exhibits a distorted octahedral geometry, whereas in the $^3MC_{eq}$ state, the coordination of Ir decreases from 6 to 5 due to the Ir–N_{N^N} elongation and rotation, globally displaying a distorted trigonal bipyramidal geometry around the Ir atom. As for the $^3MC_{ax}$ state minima, the strong geometrical distortion suffered by the system at the $^3MC_{eq}$ minima also leads to a much smaller gap with the ground state and the presence of accessible T_1/S_0 STC regions. Regarding their energy positions, it is important to stress that in all the cases reported in the literature, the $^3MC_{eq}$ state appears to be lower in energy than the $^3MC_{ax}$ one, consequently making its involvement in principle more relevant than that of the $^3MC_{ax}$ state.[18–24] As a final remark, similar MC states were also found while studying the photorelease of N^N ligands in some complexes of the $[Ru(N^N)_3]^{2+}$ family.[25–29]

In the present work, the photophysical properties of $[Ir(ppy)_2(bpy)]^+$, $[Ir(ppy)_2(pbpy)]^+$ and $[Ir(ppy)_2(dpbpy)]^+$ (hereafter complexes **1**, **2** and **3**, respectively, see Fig. 1) were studied theoretically through density functional theory (DFT) and time-dependent DFT (TD-DFT) calculations. The main aim is to explain the different emission quantum yields exhibited by these complexes in CH_2Cl_2 solution (0.196, 0.049 and 0.036 for **1**, **2** and **3**, respectively).[12,13] In a previous study, Accorsi, Ortí and coworkers concluded that the different quantum yields could be explained by the reduction of the adiabatic energy difference between the minimum-energy geometries of the non-emitting $^3MC_{ax}$ state and the emitting metal-to-ligand charge transfer (^3MLCT) state, which indeed decreased along the series.[13] By performing thorough characterization of the potential energy surface (PES) involving the lowest-energy excited triplet states, we now conclude that the $^3MC_{eq}$ states, which were not considered previously, play a fundamental role in the non-radiative decay of this family of Ir complexes.

Computational details

The energy minima of all the triplet and singlet states of complexes **1–3** were calculated at the DFT level of theory by optimizing the molecular geometry without imposing any symmetry constraints. Becke's three-parameter exchange–correlation B3LYP functional[30,31] was selected, which was previously employed, successfully, for these and other Ir cationic complexes.[12,13] As a basis set, the DEF2-SVP basis was used for all the atoms in the systems.[32–34] All calculations were carried out employing the Orca software (in its 5.0.1 version).[35] The inner core electrons of Ir were substituted by the Stuttgart–Dresden effective core potential while explicitly treating the outer core $[(5s)^2(5p)^6]$ and the $(5d)^6$ valence electrons. For the calculations implying triplet states, the unrestricted UDFT approximation was used, checking that the spin contamination was, always, between 1.95 and 2.05. Frequency calculations were carried out to guarantee that all the optimized geometries have no imaginary frequency and therefore correspond to true minima. Solvent (CH_2Cl_2) effects were included in all the calculations using the conductor-like polarizable continuum model (CPCM).[36] To assign the nature of the different excited triplet states, TD-DFT calculations, at the same level of theory, were carried out as implemented in Orca 5. To facilitate this assignment, natural transition orbitals (NTOs)[37] were obtained at the B3LYP/DEF2-SVP level for the minima computed with Orca 5 for the different excited states using the Gaussian 16 software (Rev. A.03)[38] and the polarized continuum model (PCM) to simulate the solvent effects.[39] The climbing image nudged elastic band (CI-NEB)[40] method was employed, as implemented in Orca, to find the minimum energy paths (MEPs) connecting the minima of the different excited states and also the climbing image (CI) along them (Fig. S28†). Starting from these structures, the corresponding transition states (TSs) were optimized (Fig. S29†). The Orca software was also employed for the optimization of the minimum-energy crossing points (MECPs) for singlet/triplet crossings (STC-MECPs).

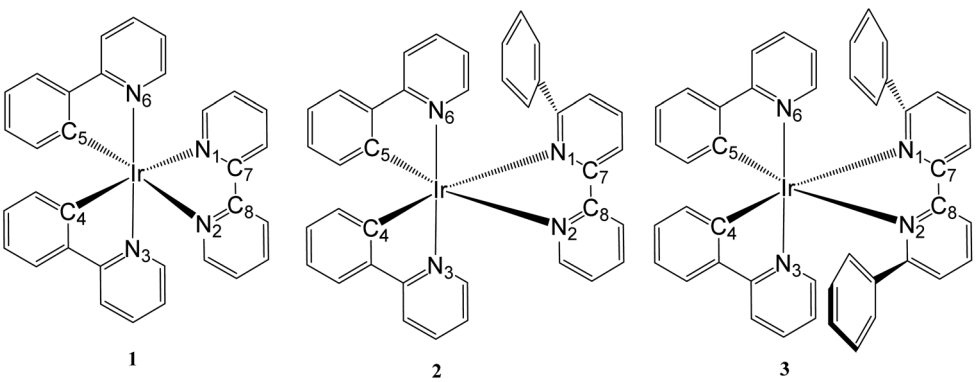

Fig. 1 Chemical structures of the Ir(III) complexes studied in this work, $[Ir(ppy)_2(bpy)]^+$ (**1**), $[Ir(ppy)_2(pbpy)]^+$ (**2**) and $[Ir(ppy)_2(dpbpy)]^+$ (**3**).

Results and discussion

Radiative decay of complexes 1–3

The electronic ground-state minima, hereafter $(S_0)_{min}$, of complexes **1–3** were localized by optimizing the geometry of the complexes at the DFT/B3LYP-DEF2-SVP level of theory including solvent effects using the CPCM method. The optimized bond distances defining the coordination sphere of Ir in $(S_0)_{min}$, together with those obtained for the different excited states discussed below, are summarized in Table 1, and appear to be in agreement with previous theoretical (Table S1, ESI†) and experimental data.[13] The three complexes present a near octahedral coordination of the Ir atom in S_0 (Fig. S1, ESI†), although the symmetry of the $(S_0)_{min}$ structure decreases on passing from **1** to complexes **2** and **3**. Whereas for complex **1**, the two Ir–N_{bpy} distances are equal, significant differences appear between them for the corresponding minima of **2** and **3** (Table 1). Smaller differences are found for the two Ir–N_{ppy} and two Ir–C_{ppy} bonds. In addition, the attachment of phenyl rings to the bpy ligand in complex **2** or **3** induces an internal twisting around the interring bond of the bpy of 15.13° and 35.30° for complexes **2** and **3**, respectively (dihedral angle N_1–C_7–C_8–N_2 in Fig. 1). Instead, for complex **1**, the bpy ligand remains mostly planar (N_1–C_7–C_8–N_2 = 1.74°).

Regarding the electronic structure of these complexes, Fig. 2 shows the frontier MOs calculated for complex **1** at the ground state $(S_0)_{min}$ geometry, which are relevant for the description of the lowest triplet excited states listed in Table 2. The e_g* MO (LUMO+10), whose population is responsible for the strong distortion of the Ir–N_{ppy} bonds leading to the MC_{ax} excited states, is also included in Fig. 2. The frontier MOs of complexes **2** and **3** display similar topologies to those calcu-

Table 1 DFT B3LYP/DEF2-SVP-CPCM(CH_2Cl_2) optimized bond lengths (in Å) computed for the energy minima of the different electronic states characterized for complexes **1**, **2** and **3**

	Bond[a]	$(S_0)_{min}$	$(^3MLCT)_{min}$	$(^3MC_{ax\ 1})_{min}$	$(^3MC_{ax\ 2})_{min}$	$(^3MC_{eq\ 1})_{min}$	$(^3MC_{eq\ 2})_{min}$
Complex **1**	Ir–$N_{1\text{-bpy}}$	2.218	2.203	2.229	2.232	3.272	—
	Ir–$N_{2\text{-bpy}}$	2.218	2.203	2.260	2.232	2.312	—
	Ir–$N_{3\text{-ppy}}$	2.090	2.090	2.292	2.493	2.081	—
	Ir–$N_{6\text{-ppy}}$	2.090	2.090	2.610	2.493	2.084	—
	Ir–$C_{4\text{-ppy}}$	2.029	2.007	2.044	2.028	2.065	—
	Ir–$C_{5\text{-ppy}}$	2.029	2.007	2.040	2.028	2.041	—
Complex **2**	Ir–$N_{1\text{-bpy}}$	2.358	2.236	2.297	2.464	3.642	2.399
	Ir–$N_{2\text{-bpy}}$	2.214	2.232	2.247	2.233	2.294	3.534
	Ir–$N_{3\text{-ppy}}$	2.099	2.095	2.295	2.582	2.082	2.094
	Ir–$N_{6\text{-ppy}}$	2.083	2.084	2.646	2.233	2.085	2.080
	Ir–$C_{4\text{-ppy}}$	2.018	2.027	2.036	2.047	2.066	2.048
	Ir–$C_{5\text{-ppy}}$	2.034	1.992	2.049	2.043	2.045	2.045
Complex **3**	Ir–$N_{1\text{-bpy}}$	2.369	2.305	2.303	—	3.674	—
	Ir–$N_{2\text{-bpy}}$	2.346	2.238	2.456	—	2.402	—
	Ir–$N_{3\text{-ppy}}$	2.085	2.083	2.225	—	2.079	—
	Ir–$N_{6\text{-ppy}}$	2.089	2.100	2.623	—	2.094	—
	Ir–$C_{4\text{-ppy}}$	2.022	1.996	2.036	—	2.045	—
	Ir–$C_{5\text{-ppy}}$	2.026	2.020	2.054	—	2.049	—

[a] Atomic numbering follows that given in Fig. 1.

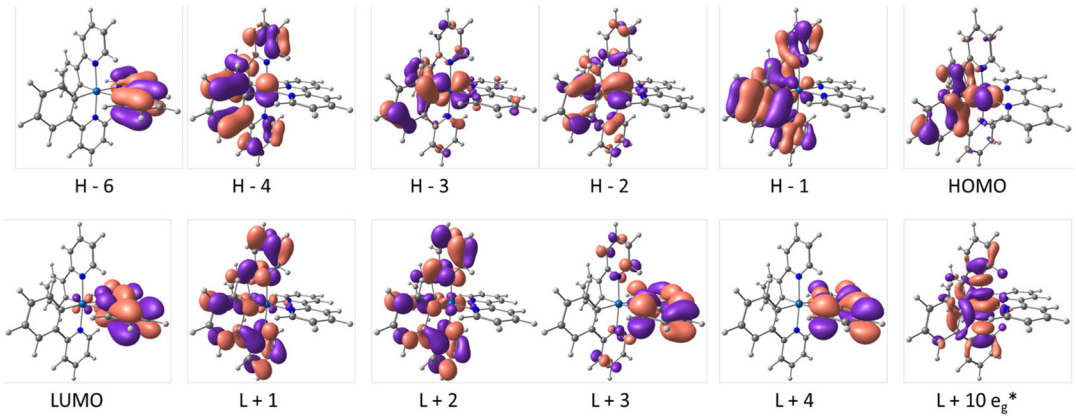

Fig. 2 Isosurface contour plots (±0.03 a.u.) computed for the molecular orbitals of complex **1** at DFT B3LYP/DEF2-SVP-CPCM(CH_2Cl_2). See Fig. S2 and S3 in the ESI† for the molecular orbitals of complexes **2** and **3**.

Table 2 TDDFT B3LYP/DEF2-SVP-CPCM(CH_2Cl_2) low-lying triplet excited states calculated at the $(S_0)_{min}$ geometries for complexes **1–3**. H and L denote the HOMO and LUMO, respectively

	State	E (eV)	Monoexcitation (%)	Nature
Complex **1**	T_1 (^{3}MLCT)	2.50	H → L (98)	MLCT/LLCT
	T_2	2.74	H → L+1 (66)	LC_{ppy}/MLCT
			H−1 → L+2 (16)	
	T_3	2.78	H → L+2 (54)	LC_{ppy}/MLCT
			H−1 → L+1 (25)	
	T_4	2.93	H−2 → L (40)	LC_{bpy}/MLCT/LLCT
			H−6 → L (34)	
			H−4 → L (11)	
	T_5	3.08	H−3 → L (54)	MLCT/LLCT
			H−1 → L (31)	
	T_6	3.18	H → L+1 (27)	LC_{ppy}/MLCT/LLCT
			H−2 → L+1 (20)	
			H−1 → L+1 (15)	
Complex **2**	T_1 (^{3}MLCT)	2.54	H → L (95)	MLCT/LLCT
	T_2	2.71	H → L+1 (53)	LC_{ppy}/MLCT
			H−1 → L+2 (11)	
			H → L+2 (11)	
	T_3	2.77	H → L+2 (34)	LC_{ppy}/MLCT
			H−1 → L+1 (26)	
	T_4	2.91	H−2 → L (36)	LC_{bpy}/MLCT/LLCT
			H−8 → L (16)	
			H−6 → L (15)	
	T_5	3.13	H−3 → L (42)	MLCT/LLCT
			H−1 → L (35)	
	T_6	3.14	H−2 → L+1 (19)	LC_{ppy}/MLCT/LLCT
			H → L+1 (17)	
Complex **3**	T_1 (^{3}MLCT)	2.58	H → L (66)	MLCT/LLCT
			H → L+1 (15)	
	T_2	2.74	H → L+1 (17)	LC_{ppy}/MLCT
			H → L+2 (15)	
			H−1 → L+1 (15)	
			H → L+3 (13)	
	T_3	2.79	H → L (25)	LC_{ppy}/MLCT
			H → L+2 (22)	
			H → L+1 (19)	
	T_4	3.03	H−2 → L (21)	LC_{bpy}/MLCT/LLCT
			H−6 → L (11)	
	T_5	3.15	H−2 → L (22)	MLCT/LLCT
			H → L+2 (22)	
			H−2 → L+2 (11)	
	T_6	3.16	H−5 → L (14)	MLCT/LLCT/LLCT
			H−4 → L (10)	

lated for **1**, but now the e_g* MO corresponds to the LUMO+12 and LUMO+14, respectively (Fig. S2 and S3, ESI†). At the $(S_0)_{min}$ minima, no e_g* MO that could be associated with the MC_{eq} state was found. The HOMO in the three complexes is composed of the d orbitals of Ir and the π orbitals from the ppy ligands, mostly from the phenyl rings. In contrast, the LUMO is localized on the auxiliary N^N ligand and corresponds in the three cases to the π* LUMO of bpy, as expected for these cyclometallated Ir complexes. The energy gap between the HOMO and LUMO increases along the series (3.21, 3.26 and 3.42 eV for **1**, **2** and **3**, respectively). This increment is mainly produced by the destabilization of the LUMO (−2.64, −2.60 and −2.45 eV, respectively) as a consequence of the attachment of phenyls rings to the ancillary ligand, which induces a rotation of the ligand around the interring bond, thus reducing the conjugation between the pyridine rings.

The excited triplet states of the three complexes were first investigated by performing TD-DFT calculations (50 roots) at the ground state minimum-energy $(S_0)_{min}$ geometries (Table 2). The electronic nature of the lowest-lying triplet states at $(S_0)_{min}$ was first determined by analyzing the monoelectronic excitations contributing to the wave function of the state with a weight higher than 10%, and confirmed by NTO analysis (see Fig. S4–S6† to visualize the NTOs calculated for states T_1, T_2 and T_3 of complexes **1**, **2** and **3**, respectively). As expected, the lowest triplet state (T_1) results in the three complexes from the HOMO → LUMO excitation, which implies an electron transfer from the Ir atom and the phenyl rings of the ppy ligands to the ancillary bpy ligand. The T_1 state thus exhibits a mixed metal-to-ligand/ligand-to-ligand charge transfer (^{3}MLCT/^{3}LLCT) nature and will be hereafter named ^{3}MLCT. The T_2 and T_3 states possess a ligand-centered ($^3LC_{ppy}$) character, and result from the HOMO−1, HOMO → LUMO+1, LUMO+2 excitations (Table 2) that mainly involve the ppy ligand with little contribution from the metal (Fig. 2 and Fig. S2–S3, ESI†). These states are around 0.2 eV higher in energy than the T_1 state (Table 2). The T_4 state shows a ligand-centered character involving the bpy ligand ($^3LC_{bpy}$) combined with the ^{3}MLCT/^{3}LLCT character and is located for all complexes around 0.4 eV above the T_1 state. The T_5 state shows a ^{3}MLCT/^{3}LLCT nature, and T_6 has a $^3LC_{ppy}$ character combined with ^{3}MLCT/^{3}LLCT.

The energy minima of the ^{3}MLCT T_1 state of complexes **1–3**, hereafter $(^3MLCT)_{min}$, were characterized by optimizing the geometry of the complex at the UDFT B3LYP/DEF2-SVP-CPCM(CH_2Cl_2) level of theory using a spin multiplicity value of 3. The spin density plots shown in Fig. S7† and the NTO in Fig. S8,† with one unpaired electron residing on the phenyl rings and the Ir atom and the other unpaired electron on the bpy ligand, confirm the ^{3}MLCT/^{3}LLCT nature of the T_1 state of the three complexes. The equilibrium $(^3MLCT)_{min}$ structures are similar to those obtained for the $(S_0)_{min}$ minima, maintaining the near octahedral coordination of Ir (see Table 1 and Fig. S1, ESI†). The geometrical parameters calculated for $(^3MLCT)_{min}$ also show lower symmetry for complexes **2** and **3** compared to those of **1**. Due to the population of the LUMO, spreading over the N^N ligand as mentioned before, the bpy ligand becomes more planar in the ^{3}MLCT state than that in S_0, with the N_1–C_7–C_8–N_2 dihedral structure having values of 0.98°, 8.72° and 1.59° for **1**, **2** and **3**, respectively. Compared to S_0, for which the N_1–C_7–C_8–N_2 angle has values of 1.74°, 15.13° and 35.30°, respectively, the planarization of the bpy ligand in complex **3** is nearly complete and much more relevant than that for complex **2**. In addition, the dihedral angle Ir–N_1–N_2–C_8, defining the bending of the bpy ligand with respect to the equatorial plane of the complex, also increases along the series **1** (0.26°), **2** (17.07°) and **3** (26.98°), showing the distortion from the octahedral structure (Fig. 3).

The energy gap between the T_1 and S_0 states was vertically computed at the optimized $(^3MLCT)_{min}$ geometry to estimate the emission energy. Similar energy gaps of 2.06, 2.00 and 2.02

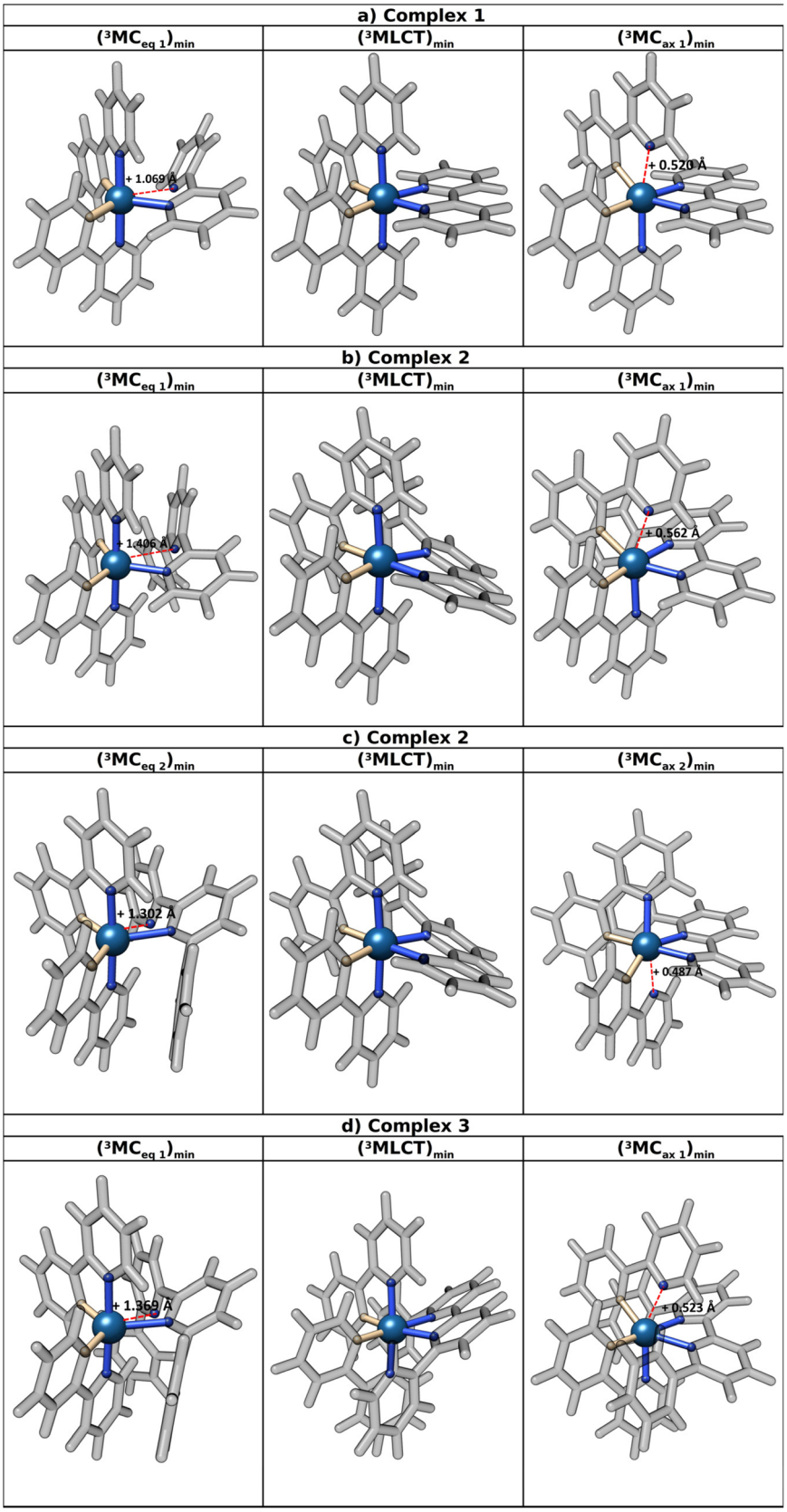

Fig. 3 B3LYP/DEF2-SVP-CPCM(CH_2Cl_2)-optimized geometries for the ^{3}MLCT, $^3MC_{ax}$ and $^3MC_{eq}$ states of complexes **1** (a), **2** (b and c) and **3** (d). Differences in selected bond lengths (dashed red lines) with respect to the $(^3MLCT)_{min}$ minima, highlighting the main geometrical deformations characterizing the $^3MC_{ax}$ and $^3MC_{eq}$ minima, are reported in Å.

eV were obtained for complexes **1**, **2** and **3**, respectively. These values are in good agreement with the experimental emission energy maxima (2.08, 2.02 and 2.09 eV),[13] thus supporting the computational approach employed in this work and the assignment of the ^{3}MLCT T_1 state as the emissive state. Based on these results, it is possible to conclude that the same radiative decay path involving the ^{3}MLCT state is in operation for the three complexes. The differences observed in the emission quantum yields reported experimentally for complexes **1–3** should be the result of different efficiencies in the non-radiative decay paths.

Non-radiative decay of complexes 1–3

According to the previous work of Accorsi, Ortí and coworkers,[13] it was proposed that the difference in the emission quantum yield of complexes **1** (0.196), **2** (0.049) and **3** (0.036) was due to the difference in their ability to reach the $^3MC_{ax}$ state from $(^3MLCT)_{min}$, evaluated as the energy difference between the ^{3}MLCT and $^3MC_{ax}$ minima. In fact, according to the Frank–Condon principle and the strong spin–orbit coupling characterizing Ir complexes, most of the excited population is supposed to decay to the ^{3}MLCT minimum, which can be considered as the starting point for all the decay processes. We can now map the PES between the ^{3}MLCT and $^3MC_{ax}$ minima and to localize the MECP between the S_0 and ^{3}MC states, for evaluating the non-radiative decay process through $^3MC_{ax}$ and its barriers.

Starting from the $(^3MLCT)_{min}$ geometries, the $^3MC_{ax}$ energy minima, hereafter $(^3MC_{ax\ 1})_{min}$, were localized by geometry optimization at the DFT level (Fig. S9†). The obtained minima are non-symmetric since they mainly involve the elongation of one Ir–N_{ppy} bond, which lengthens with respect to the $(^3MLCT)_{min}$ geometry by 0.520, 0.562 and 0.523 Å in complexes **1**, **2** and **3**, respectively (Table 1 and Fig. 3). By comparing the obtained structures with those published by Accorsi, Ortí and coworkers,[13] both similarities and significant differences have been noted (see Table S1†). The most important point is that in their work, the ^{3}MC minimum of complex **1** presents a symmetric structure characterized by the same elongation of both Ir–N_{ppy} bonds (leading to 2.505 Å bond distances). In contrast, in the here-optimized $(^3MC_{ax\ 1})_{min}$ structure, although again both Ir–N_{ppy} bonds are significantly enlarged, one displays a much higher value (2.610 Å) than the other (2.292 Å). In order to verify if that could be a consequence of the different computational details employed in the two studies, the ^{3}MC structure reported by Accorsi, Ortí and coworkers was here re-optimized leading to a symmetric ^{3}MC minimum, hereafter $(^3MC_{ax\ 2})_{min}$, characterized by equal Ir–N_{ppy} bond distances of 2.493 Å. Regarding complexes **2** and **3**, our calculations provide asymmetric structures similar to those previously reported (Table S1†),[13] in which both Ir–N_{ppy} bonds are elongated, but one much more than the other (Table 1 and Fig. S9†). Some differences can however be noticed regarding the Ir–N_{bpy} distances, particularly in complex **2**, where one Ir–N_{bpy} bond is 0.051 Å shorter than the value previously calculated (Table S1†). Any attempt to optimize in complexes **2** and **3** a $^3MC_{ax}$ structure having equal Ir–N_{ppy} bond distances failed. An additional factor affecting complex **2** is that, due to its lower symmetry, two non-equivalent $^3MC_{ax}$ minima, $(^3MC_{ax\ 1})_{min}$ and $(^3MC_{ax\ 2})_{min}$, are possible, depending on which of the two Ir–N_{ppy} bonds is elongated (Table 1, Fig. 3 and Fig. S9†).

Altogether, we have characterized the following $^3MC_{ax}$ minima in our three complexes (Fig. S9†). Two minima are observed for complex **1**: $(^3MC_{ax\ 1})_{min}$, having one Ir–N_{ppy} much longer than the other, and $(^3MC_{ax\ 2})_{min}$, having equal Ir–N_{ppy} bonds. Two minima are observed for complex **2**, $(^3MC_{ax\ 1})_{min}$ and $(^3MC_{ax\ 2})_{min}$, depending on which Ir–N_{ppy} bond is the one most significantly lengthened. One minimum is observed for complex **3**, again characterized by one Ir–N_{ppy} bond distance remarkably longer than the other. The nature of the ^{3}MC states of all these minima was confirmed by computing the corresponding spin densities (Fig. S10†) and NTOs (Fig. S11†).

Once the $^3MC_{ax}$ structures were optimized, their energies were computed to evaluate their importance in the photophysics of complexes **1–3**. Table 3 summarizes the relative energies of all the triplet structures characterized for the three complexes, whereas Fig. 4 (right side) shows the MEPs connecting the triplet states most relevant for the decay along the $^3MC_{ax}$. The adiabatic energy differences between the $^3MC_{ax}$ and ^{3}MLCT minima are 0.61/0.67 ($^3MC_{ax\ 1}$ and $^3MC_{ax\ 2}$), 0.48/0.55 ($^3MC_{ax\ 1}$ and $^3MC_{ax\ 2}$) and 0.28 eV for complexes **1**, **2** and **3**, respectively. Despite the mentioned geometrical differences, these relative energies are in agreement with those previously reported by Accorsi, Ortí and coworkers (0.60, 0.50 and 0.20 eV, respectively) and, in principle, justify the hypothesis of relating the decrease in the emission quantum yield to an increase in the accessibility of the $^3MC_{ax}$-mediated non-radiative decay path. It is however important to notice that, although the trend in the energies is consistent with such an interpretation, the so-computed energy difference for complex **2** is much more similar to that obtained for complex **1** than to the one characterizing complex **3**. This indeed is in contrast to the fact that complexes **2** and **3** have much similar emission quantum yields (0049 and 0.036, respectively) significantly lower than that of complex **1** (0.196). This might be an indication of the limitation of evaluating the viability of the process by just computing the energy difference between the final and initial points, which does not account for any possible barriers along the path.

To properly evaluate the energy barriers leading to the $^3MC_{ax}$ minima, the corresponding TSs between the $(^3MLCT)_{min}$ and $(^3MC_{ax})_{min}$ structures, hereafter $(^3MLCT/^3MC_{ax})_{ts}$ (see Fig. S12†), were optimized using as a starting geometry the so-called climbing image (hereafter $(^3MLCT/^3MC_{ax})_{CI\text{-}NEB}$, Fig. S13†) obtained from the CI-NEB calculations between the two mentioned minima. All obtained TSs display a single imaginary frequency describing the corresponding geometrical deformation connecting the two minima (see Fig. S14–S17†). For complex **3**, the corresponding TS is also characterized by an imaginary frequency displaying the expected elongation of one Ir–N_{ppy} bond, but the structure shows an unexpected significant elongation of one Ir–N_{bpy}

Table 3 DFT B3LYP/DEF2-SVP-CPCM(CH_2Cl_2) relative energies (in eV) computed for the S_0 and T_1 states at all the critical points characterized for complexes **1**, **2** and **3**[a]

	Geometry	S_0	T_1
Complex **1**	$(S_0)_{min}$	0.00	2.59
	$(^3MLCT)_{min}$	0.27	2.34
	$(^3MLCT/^3MC_{ax\ 1})_{ts}$	1.35	3.10
	$(^3MC_{ax\ 1})_{min}$	2.43	2.95
	$(^3MC_{ax\ 1}/S_0)_{stc\text{-}mecp}$	2.99	2.99
	$(^3MC_{ax\ 2})_{min}$	1.52	3.01
	$(^3MC_{ax\ 2}/S_0)_{stc\text{-}mecp}$	3.28	3.28
	$(^3MLCT/^3MC_{eq\ 1})_{ts}$	2.40	2.95
	$(^3MC_{eq\ 1})_{min}$	2.44	2.95
	$(^3MC_{eq\ 1}/S_0)_{stc\text{-}mecp}$	2.96	2.97
Complex **2**	$(S_0)_{min}$	0.00	2.63
	$(^3MLCT)_{min}$	0.32	2.32
	$(^3MLCT/^3MC_{ax\ 1})_{ts}$	1.24	2.99
	$(^3MC_{ax\ 1})_{min}$	2.80	2.80
	$(^3MC_{ax\ 1}/S_0)_{stc\text{-}mecp}$	2.81	2.81
	$(^3MLCT/^3MC_{eq\ 1})_{ts}$	0.54	2.62
	$(^3MC_{eq\ 1})_{min}$	2.21	2.45
	$(^3MC_{eq\ 1}/S_0)_{stc\text{-}mecp}$	2.45	2.45
	$(^3MLCT/^3MC_{ax\ 2})_{ts}$	1.13	3.02
	$(^3MC_{ax\ 2})_{min}$	2.35	2.87
	$(^3MC_{ax\ 1}/S_0)_{stc\text{-}mecp}$	2.90	2.90
	$(^3MLCT/^3MC_{eq\ 2})_{CI\text{-}NEB}$	1.04	2.94
	$(^3MC_{eq\ 2})_{min}$	2.27	2.78
	$(^3MC_{eq.\ 2}/S_0)_{stc\text{-}mecp}$	2.82	2.82
Complex **3**	$(S_0)_{min}$	0.00	2.68
	$(^3MLCT)_{min}$	0.37	2.40
	$(^3MLCT/^3MC_{ax\ 1})_{ts}$	0.99	2.86
	$(^3MC_{ax\ 1})_{min}$	2.42	2.68
	$(^3MC_{ax\ 1}/S_0)_{stc\text{-}mecp}$	2.69	2.69
	$(^3MLCT/^3MC_{eq\ 1})_{ts}$	0.38	2.56
	$(^3MC_{eq\ 1})_{min}$	1.75	2.21
	$(^3MC_{eq\ 1}/S_0)_{stc\text{-}mecp}$	2.25	2.25

[a] All reported energies are referred with respect to the S_0 energy computed at the $(S_0)_{min}$ of the corresponding complex. It is worth noting that T_1 refers to the lowest-energy triplet state at the respective geometry (Fig. 4).

bond, significantly larger than that in the $(^3MC_{ax\ 1})_{min}$ structure. Using such TSs, but keeping in mind the limitations reported for the TS of complex **3**, the barriers from $(^3MLCT)_{min}$ to $(^3MC_{ax})_{min}$ are equal to 0.76, 0.67/0.70 and 0.46 eV for complexes **1**, **2** and **3**, respectively (Fig. 4, right). These values confirm the increasing ability of reaching the $^3MC_{ax}$ minima along the present series of complexes, in agreement with the decrease of the emission quantum yield along the series. However, as for the adiabatic energy differences, the barrier computed for complex **2** is much more similar to that of complex **1** than to the one computed for complex **3**.

The second step in the non-radiative decay path mediated by the $^3MC_{ax}$ state is the passage from the $(^3MC_{ax})_{min}$ minima to the $^3MC_{ax}/S_0$ MECP, hereafter $(^3MC_{ax}/S_0)_{stc\text{-}mecp}$, leading back to the ground state. From the characterized $^3MC_{ax}$ minima, geometrically close $^3MC_{ax}/S_0$ MECPs (Fig. S18†) were localized at 0.04 $(^3MC_{ax\ 1})$/0.27 $(^3MC_{ax\ 2})$, 0.01 $(^3MC_{ax\ 1})$/0.03 $(^3MC_{ax\ 2})$, and 0.01 eV for complexes **1**, **2** and **3**, respectively (Fig. 4, right). Then, complex **1** has to surmount the non-negligible barrier of 0.27 eV to reach the $^3MC_{ax}/S_0$ MECP closer to the $(^3MC_{ax\ 2})_{min}$ geometry, whereas all other $^3MC_{ax}$ minima are almost degenerate with their corresponding $(^3MC_{ax}/S_0)_{stc\text{-}mecp}$. These results are in agreement with the recent work of Luo *et al.* on a different family of Ir complexes,[41] where it was also concluded that the $(^3MC_{ax})_{min}$ minima are almost degenerate (<2 kcal mol^{-1}) with their $(^3MC_{ax}/S_0)_{stc\text{-}mecp}$ structures. The higher difference from the $(^3MC_{ax\ 2})_{min}$ structure is in line with the much higher S_0/T_1 energy gap characterizing complex **1** at such a geometry (1.49 eV, Table 3) with respect to the remaining $^3MC_{ax}$ minima, displaying a S_0/T_1 gap of no more than 0.6 eV. With that in mind and taking into account that the more symmetric $(^3MC_{ax\ 2})_{min}$ structure is 0.06 eV higher in energy than the $(^3MC_{ax\ 1})_{min}$ structure, we consider that the latter plays a much prominent role in the photophysics of complex **1** than the former, which will not be further discussed here.

Having localized the different $^3MC/S_0$ MECPs, it is feasible to evaluate the accessibility of the non-radiative decay process by computing both what we call the global energy barrier (the sum of the barrier to reach the $^3MC_{ax}$ minimum from the $(^3MLCT)_{min}$ and the barrier to the corresponding T_1/S_0 MECP) and the energy difference between the $(^3MLCT)_{min}$ and $(^3MC_{ax}/S_0)_{stc\text{-}mecp}$ structures. Due to the negligible energy separation between the $^3MC_{ax}$ minima and the T_1/S_0 MECPs, in the present case, the computation of this separation is not very informative, so we can base our evaluation of the $^3MC_{ax}$-mediated non-radiative decay process using the previously stated barriers from the $(^3MLCT)_{min}$ to the $(^3MC_{ax})_{min}$.

Since the different ability to evolve along the non-radiative decay mediated by the $^3MC_{ax}$ states can only partially explain the experimental differences in the emission quantum yields of complexes **1–3**, we also studied the existence of $^3MC_{eq}$ states and their importance in the photophysical properties. To optimize the corresponding minima, hereafter $(^3MC_{eq})_{min}$, one Ir–N_{bpy} bond was elongated and, in some cases, the dihedral angle (N_1–C_7–C_8–N_2) defining the coplanarity of the two pyridine rings in the bpy ligand was rotated to reduce the coordination of the Ir atom from six to five. In all cases, even in those in which the starting geometry has an Ir coordination of six, the obtained $(^3MC_{eq})_{min}$ minima display a distorted trigonal bipyramidal geometry around the Ir atom, in which one Ir–N_{bpy} bond distance is around 2.3–2.4 Å and the other Ir–N_{bpy} distance is much longer (3.3–3.7 Å) due to the internal rotation of the pyridine ring (see Table 1, Fig. S19† and Fig. 3). As for the $^3MC_{ax}$ state, two $(^3MC_{eq})_{min}$ minima are found for complex **2**, each one associated with the elongation of one of the two non-equivalent Ir–N_{bpy} bonds. The $(^3MC_{eq\ 1})_{min}$ structure implies the elongation of the Ir–N_{bpy} bond involving the pyridine ring substituted with the phenyl ring, and the $(^3MC_{eq\ 2})_{min}$ results from the elongation of the Ir–N_{bpy} bond of the unsubstituted pyridine ring. The structure and electronic nature of the $(^3MC_{eq})_{min}$ minima found for complexes **1–3** are similar to those previously reported, for a different $[Ir(C\hat{}N)_3]$ family of complexes, by Treboux and coworkers and by Djurovich, Thomson and coworkers.[42,43]

Altogether, we have characterized the following $^3MC_{eq}$ minima in our three complexes (Fig. S19†). One minimum for complex **1**, $(^3MC_{eq\ 1})_{min}$, having one Ir–N_{bpy} much longer than

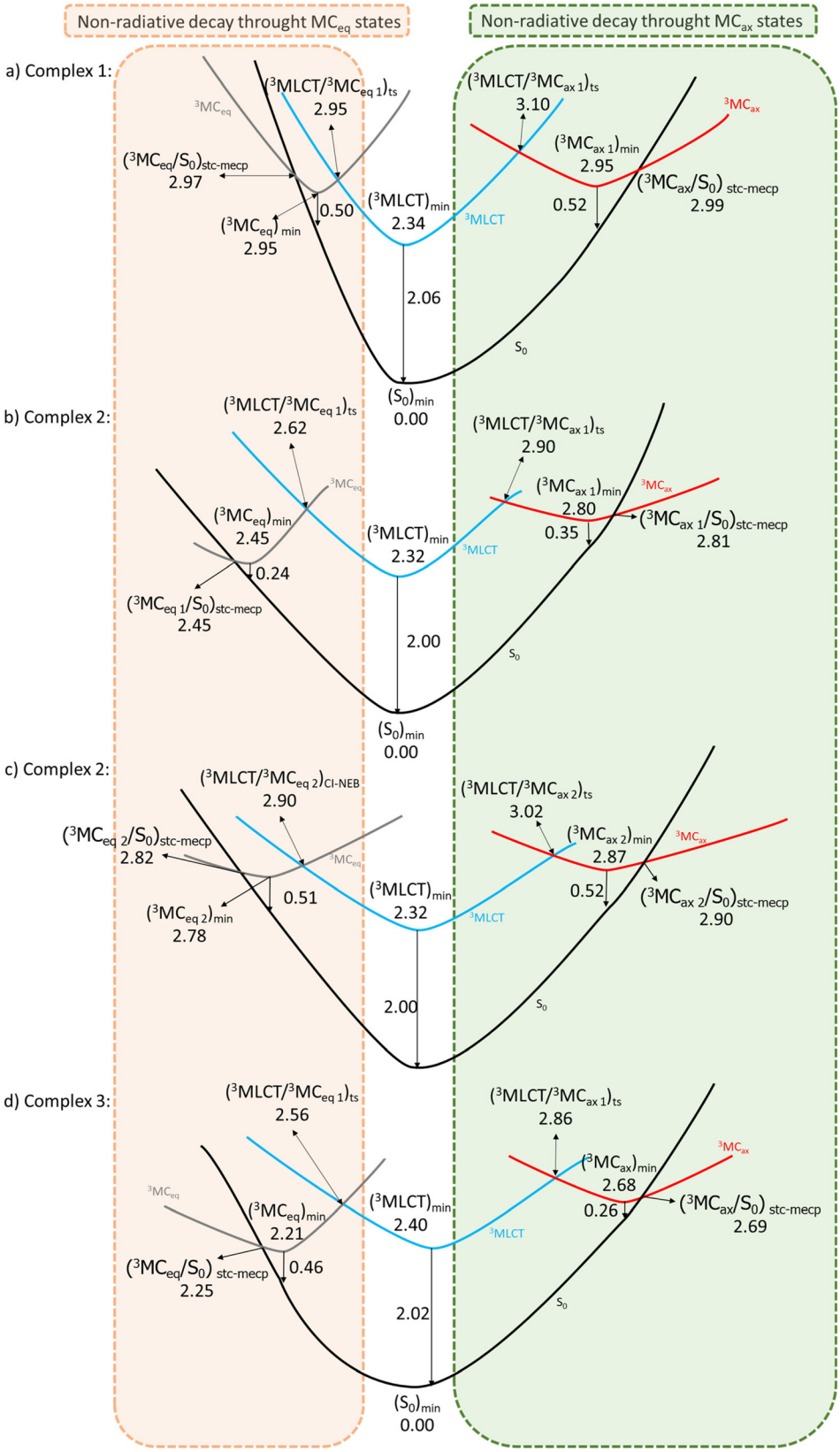

Fig. 4 Schematic representation of the characterized photophysics of complexes **1** (a), **2** (b and c) and **3** (d). The left side (in orange box) shows the non-radiative decay path through the MC_{eq} states. The right side (in green box) shows the non-radiative decay path through the MC_{ax} states. All the reported energies are in eV and have been computed at the DFT B3LYP/DEF2-SVP-CPCM(CH_2Cl_2) level.

the other. Two minima for complex **2**, $(^3MC_{eq\ 1})_{min}$ and $(^3MC_{eq\ 2})_{min}$, depending on which Ir–N_{bpy} bond is the one most significantly lengthened. One minimum for complex **3**, again characterized by one Ir–N_{bpy} bond distance remarkably longer than the other. The ^3MC nature of the triplet state in all these minima was confirmed by computing the corresponding spin-densities (Fig. S20†) and NTOs (Fig. S21†).

Once the $^3MC_{eq}$ structures were optimized, the ability to decay through them was evaluated as we did for the $^3MC_{ax}$ geometries. The relative energies of all the triplet structures characterized for the three complexes are summarized in Table 3, whereas the left side of Fig. 4 shows the MEPs connecting the triplet states for the decay through the $^3MC_{eq}$ states. The adiabatic energy difference between the $(^3MC_{eq})_{min}$ and the $(^3MLCT)_{min}$ optimized structures is computed to be 0.61 eV for complex **1**, 0.13/0.46 ($^3MC_{eq\ 1}$ and $^3MC_{eq\ 2}$) for **2** and −0.18 eV for **3**, with the $^3MC_{eq}$ state being more stable than the $(^3MLCT)_{min}$ in complex **3**.

TS optimizations were performed starting from the climbing images (hereafter $(^3MLCT/^3MC_{eq})_{CI\text{-}NEB}$, Fig. S22†) obtained from CI-NEB calculations. The TSs connecting the $(^3MLCT)_{min}$ and $(^3MC_{eq})_{min}$ minima, hereafter $(^3MLCT/^3MC_{eq})_{ts}$, were found for the three complexes but for the $(^3MC_{eq\ 2})_{min}$ structure of complex **2** (Fig. S23†). The latter was then approximated as the obtained climbing image. The TSs were characterized by a small imaginary frequency, whose associated displacement vectors define the rotation of one pyridine ring of the bpy ligand leading to the dissociation of the Ir–N_{bpy} bond and to the geometrical change from a six-coordinated octahedral structure to a five-coordinated trigonal–bipyramidal structure (Fig. S24–26†). Using such TSs (and the climbing image structure as an approximation of the TS connecting the $(^3MC_{eq\ 2})_{min}$ in complex **2**), the barriers from $(^3MLCT)_{min}$ to $(^3MC_{eq})_{min}$ are equal to 0.61, 0.30/0.58 and 0.17 eV for complexes **1**, **2** and **3**, respectively. These values justify a decrease in the quantum yield along the series, even predicting a lower value for complex **3** than that for complex **2**.

Similar to the $^3MC_{ax}$ minima, almost degenerate $^3MC/S_0$ MECPs, hereafter $(^3MC_{eq}/S_0)_{stc\text{-}mecp}$, were characterized geometrically near the $^3MC_{eq}$ minima (Fig. S27†). These MECPs are indeed localized 0.02, 0.00/0.04 ($^3MC_{eq\ 1}$ and $^3MC_{eq\ 2}$) and 0.04 eV higher than the $^3MC_{eq}$ minima of complexes **1**, **2** and **3**, respectively. Consequently, as for the $^3MC_{ax}$-mediated non-radiative decay, also in this case, the efficiency of the process can be evaluated only on the basis of the ability to reach the $^3MC_{eq}$ minima through the respective TS.

At this point, we are in the position to compare the non-radiative decay path mediated by the $^3MC_{ax}$ states and the one passing through the $^3MC_{eq}$ states. Table 4 summarizes the barriers characterizing the $^3MC_{ax}$ and $^3MC_{eq}$ non-radiative decay paths for complexes **1–3**, evaluated according to the obtained TSs between the ^3MLCT and $^3MC_{ax}$ and $^3MC_{eq}$ minima, with the latter being almost degenerate with the corresponding $^3MC/S_0$ crossing.

On the basis of the computed TSs, both the $^3MC_{ax}$ and $^3MC_{eq}$ non-radiative decay paths display a trend in their energy barriers, diminishing on passing from **1** to **2** and to **3**, which is in agreement with the experimentally observed decrease in the emission quantum yield. However, it is important to notice that in all cases, the energy barrier to reach the $^3MC_{eq}$ minimum is significantly lower than the one for reaching the $^3MC_{ax}$ state, being 0.15, 0.37 and 0.30 eV smaller for complexes **1**, **2**, and **3**, respectively. In addition, it should be recalled that complexes **2** and **3** display very similar emission quantum yields (0.049 and 0.036), one order of magnitude lower than that of complex **1** (0.196). Therefore, similar decay barriers should be expected for complexes **2** and **3**, significantly lower than that for complex **1**. Looking at the $^3MC_{ax}$-mediated decays, the barrier for complex **2** is however much more similar to that of complex **1** (0.09 eV difference) than to the barrier for complex **3** (0.21 eV difference). Looking instead at the $^3MC_{eq}$-mediated decays, the barrier for complex **2** is much lower than that of complex **1** (0.31 eV lower), while the difference from complex **3** is not particularly pronounced (0.14 eV). Considering the higher accessibility of the $^3MC_{eq}$ minima and the better agreement that their corresponding energy barriers display with respect to the experimental emission quantum yields, we can then assume that the $^3MC_{eq}$ states will play a more prominent role in the photophysics of the here-studied complexes than the $^3MC_{ax}$ structures.

As a final point, we found it instructive to evaluate the mentioned barrier on the basis of the obtained climbing image structures and the adiabatic energy differences (see Table S2†). Using the climbing image geometries, we obtained the same decreasing trend as that obtained employing the TSs, but, compared to the latter, the differences between the barriers of the different decay paths appeared much reduced. For instance, the energy difference between the $^3MC_{ax}$-mediated decay paths in complexes **1** and **3** (0.16 eV) is smaller than that obtained using the corresponding TSs (0.30 eV). A significant decrease is also observed between the $^3MC_{eq}$-mediated decay paths in complexes **1** and **3**, although in this case, a clear difference is still appreciable (0.32 eV). Using the adiabatic energy differences between the ^3MLCT and ^3MC minima, again the same decreasing trend is obtained, but again signifi-

Table 4 DFT B3LYP/DEF2-SVP-CPCM(CH_2Cl_2) energy barriers (eV) for evolving from the $(MLCT)_{min}$ minimum to the $(^3MC_{ax})_{min}$ and $(^3MC_{eq})_{min}$ minima for complexes **1**, **2** and **3**

	Complex	TS[a]
$(^3MC_{ax\ 1})_{min}$	**1**	0.76
$(^3MC_{ax\ 1})_{min}$	**2**	0.67
$(^3MC_{ax\ 2})_{min}$	**2**	0.70
$(^3MC_{ax\ 1})_{min}$	**3**	0.46
$(^3MC_{eq\ 1})_{min}$	**1**	0.61
$(^3MC_{eq\ 1})_{min}$	**2**	0.30
$(^3MC_{eq\ 2})_{min}$	**2**	0.58[b]
$(^3MC_{eq\ 1})_{min}$	**3**	0.16

[a] Energy difference between the $(MLCT)_{min}$ and the TS connecting the two minima. [b] The climbing image structure is used as an approximation of the TS.

cant differences with respect to the TS data emerged. For example, the same energy barrier now results in decaying along the $^3MC_{ax}$ and $^3MC_{eq}$ paths of complex **1**, while for complex **3** the $^3MC_{eq}$ decays will be very probable, with the $^3MC_{eq}$ minimum being even lower than the ^{3}MLCT structure. The comparison between the three different ways of evaluating the plausibility of a decay path highlights the importance of employing that through the characterization of the corresponding TSs, because even if the main feature (*i.e.*, the decreasing trend) can be observed even when using the less accurate strategies, significant differences will however emerge.

Conclusions

In the present contribution, the main radiative and non-radiative decay paths for three Ir complexes, $[Ir(ppy)_2(bpy)]^+$, $[Ir(ppy)_2(pbpy)]^+$ and $[Ir(ppy)_2(dpbpy)]^+$, have been theoretically studied by performing DFT-based calculations.

Despite their chemical similarities, complexes **2** and **3** show emission quantum yields one order of magnitude lower than that of complex **1** in CH_2Cl_2 solution. This has been previously explained as a consequence of the different abilities to decay non-radiatively through the so-called $^3MC_{ax}$ states, characterized by a strong elongation of one Ir–N_{ppy} bond. On evaluating the barrier associated with this process by the characterization of the PES leading to the $^3MC_{ax}$ minima, it has here emerged that a different ability to reach the $^3MC_{ax}$ state is most probably not the main cause that determines the reported different emission yields. Instead, a non-radiative decay mediated by the so-called $^3MC_{eq}$ states, characterized by a strong elongation of one Ir–N_{bpy} bond and the rotation of the respective pyridine ring leading to a five-coordinated trigonal–bipyramidal structure, appears to be more important in the photophysics of the studied complexes, in particular for complexes **2** and **3**. In fact, the non-radiative decay path mediated by the $^3MC_{eq}$ states is energetically more favorable than the one passing through the $^3MC_{ax}$ states.

The present contribution is a clear example of the importance of MC states in the photophysics of cyclometallated Ir(III) complexes. Even more importantly, the study evidences the prominent role that equatorial MC states can play in the non-radiative decay of cyclometallated Ir(III) complexes, a role that, in the present case, appears to be more relevant than that of the axial MC states, despite the latter type of MC states being much more studied in the literature than the equatorial MC states. Knowing the importance of the non-radiative decay mediated by $^3MC_{eq}$ states is fundamental information, since the formulation of complexes which do not favor the population of such states will in principle lead to better emission properties.

Author contributions

I. S.-D.: investigation, visualization, writing – original draft, writing – review & editing, formal analysis, and data curation; E. O.: methodology, project administration, resources, supervision, writing – review & editing, funding acquisition, formal analysis, and conceptualization; and A. G.: methodology, supervision, validation, writing – review & editing, formal analysis, and conceptualization.

Conflicts of interest

All the authors declare no conflict of interest.

Acknowledgements

The financial support by the MCIN/AEI of Spain (projects PID2021-128569NB-I00 and CEX2019-000919-M, funded by MCIN/AEI/10.13039/501100011033 and by "ERDF A way of making Europe") and the Generalitat Valenciana (PROMETEO/2020/077 and MFA/2022/017) is acknowledged. The MFA/2022/017 project is a part of the Advanced Materials programme supported by the MCIN with funding from the European Union NextGenerationEU (PRTR-C17.I1) and by Generalitat Valenciana. A. G. is thankful to the MCIN/AEI for his Juan de la Cierva (IJC2018-035123-I) fellowship funded by MCIN/AEI/10.13039/501100011033 and by the "European Union NextGenerationEU/PRTR". I. S.-D. also thanks Generalitat Valenciana for his predoctoral grant CIACIF/2021/438.

References

1 J. Slinker, D. Bernards, P. L. Houston, H. D. Abruña, S. Bernhard and G. G. Malliaras, *Chem. Commun.*, 2003, 2392–2399.
2 Q. Pei, G. Yu, C. Zhang, Y. Yang and A. J. Heeger, *Science*, 1995, **269**, 1086–1088.
3 R. D. Costa, E. Ortí, H. J. Bolink, F. Monti, G. Accorsi and N. Armaroli, *Angew. Chem., Int. Ed.*, 2012, **51**, 8178–8211.
4 A. Juris, V. Balzani, F. Barigelletti, S. Campagna, P. Belser and A. von Zelewsky, *Coord. Chem. Rev.*, 1988, **84**, 85–277.
5 D. N. Tritton, F. K. Tang, G. B. Bodedla, F. W. Lee, C. S. Kwan, K. C. F. Leung, X. Zhu and W. Y. Wong, *Coord. Chem. Rev.*, 2022, **459**, 214390.
6 K. K. W. Lo, W. K. Hui, C. K. Chung, K. H. K. Tsang, D. C. M. Ng, N. Zhu and K. K. Cheung, *Coord. Chem. Rev.*, 2005, **249**, 1434–1450.
7 F. F. Chen, Z. Q. Bian, Z. W. Liu, D. B. Nie, Z. Q. Chen and C. H. Huang, *Inorg. Chem.*, 2008, **47**, 2507–2513.
8 F. F. Chen, Z. Q. Bian, B. Lou, E. Ma, Z. W. Liu, D. B. Nie, Z. Q. Chen, J. Bian, Z. N. Chen and C. H. Huang, *Dalton Trans.*, 2008, 5577–5583.
9 Q. Zhao, F. Li, S. Liu, M. Yu, Z. Liu, T. Yi and C. Huang, *Inorg. Chem.*, 2008, **47**, 9256–9264.
10 Q. Zhao, T. Cao, F. Li, X. Li, H. Jing, T. Yi and C. Huang, *Organometallics*, 2007, **26**, 2077–2081.
11 H. Chen, Q. Zhao, Y. Wu, F. Li, H. Yang, T. Yi and C. Huang, *Inorg. Chem.*, 2007, **46**, 11075–11081.

12 I. Soriano-Díaz, E. Ortí and A. Giussani, *Inorg. Chem.*, 2021, **60**, 13222–13232.
13 R. D. Costa, F. Monti, G. Accorsi, A. Barbieri, H. J. Bolink, E. Ortí and N. Armaroli, *Inorg. Chem.*, 2011, **50**, 7229–7238.
14 A. Soupart, I. M. Dixon, F. Alary and J. L. Heully, *Theor. Chem. Acc.*, 2018, **137**, 1–11.
15 I. M. Dixon, J. L. Heully, F. Alary and P. I. P. Elliott, *Phys. Chem. Chem. Phys.*, 2017, **19**, 27765–27778.
16 C. Kreitner and K. Heinze, *Dalton Trans.*, 2016, **45**, 13631–13647.
17 A. Giussani, P. Pla, J. M. Junquera-Hernández and E. Ortí, *Dalton Trans.*, 2019, **48**, 9725–9733.
18 E. Matteucci, F. Monti, R. Mazzoni, A. Baschieri, C. Bizzarri and L. Sambri, *Inorg. Chem.*, 2018, **57**, 11673–11686.
19 X. Wang, S. Wang, F. Pan, L. He and L. Duan, *Inorg. Chem.*, 2019, **58**, 12132–12145.
20 S. Lee and W. S. Han, *Inorg. Chem. Front.*, 2020, **7**, 2396–2422.
21 M. Tian, R. Yu, M. Chen and L. He, *Dyes Pigm.*, 2021, **193**, 109477.
22 F. Monti, F. Kessler, M. Delgado, J. Frey, F. Bazzanini, G. Accorsi, N. Armaroli, H. J. Bolink, E. Ortí, R. Scopelliti, M. K. Nazeeruddin and E. Baranoff, *Inorg. Chem.*, 2013, **52**, 10292–10305.
23 F. Monti, A. Baschieri, I. Gualandi, J. J. Serrano-Pérez, J. M. Junquera-Hernández, D. Tonelli, A. Mazzanti, S. Muzzioli, S. Stagni, C. Roldan-Carmona, A. Pertegás, H. J. Bolink, E. Ortí, L. Sambri and N. Armaroli, *Inorg. Chem.*, 2014, **53**, 7709–7721.
24 Y. Song, R. Yu, M. Chen and L. He, *Inorg. Chem.*, 2021, **60**, 18804–18815.
25 A. Soupart, F. Alary, J. L. Heully, P. I. P. Elliott and I. M. Dixon, *Inorg. Chem.*, 2020, **59**, 14679–14695.
26 K. Eastham, P. A. Scattergood, D. Chu, R. Z. Boota, A. Soupart, F. Alary, I. M. Dixon, C. R. Rice, S. J. O. Hardman and P. I. P. Elliott, *Inorg. Chem.*, 2022, **61**, 19907–19924.
27 E. Baranoff, J. P. Collin, J. Furusho, Y. Furusho, A. C. Laemmel and J. P. Sauvage, *Inorg. Chem.*, 2002, **41**, 1215–1222.
28 J. P. Collin, D. Jouvenot, M. Koizumi and J. P. Sauvage, *Inorg. Chem.*, 2005, **44**, 4693–4698.
29 B. S. Howerton, D. K. Heidary and E. C. Glazer, *J. Am. Chem. Soc.*, 2012, **134**, 8324–8327.
30 A. D. Becke, *J. Chem. Phys.*, 1993, **98**, 5648–5652.
31 C. Lee, W. Yang and R. G. Parr, *Phys. Rev. B: Condens. Matter Mater. Phys.*, 1988, **37**, 785–789.
32 F. Weigend and R. Ahlrichs, *Phys. Chem. Chem. Phys.*, 2005, **7**, 3297.
33 F. Weigend, *Phys. Chem. Chem. Phys.*, 2006, **8**, 1057.
34 D. A. Pantazis, X.-Y. Chen, C. R. Landis and F. Neese, *J. Chem. Theory Comput.*, 2008, **4**, 908–919.
35 F. Neese, *Wiley Interdiscip. Rev.: Comput. Mol. Sci.*, 2022, **12**, e1606.
36 R. Cammi, B. Mennucci and J. Tomasi, *J. Phys. Chem. A*, 2000, **104**, 5631–5637.
37 R. L. Martin, *J. Chem. Phys.*, 2003, **118**, 4775.
38 M. J. Frisch, G. W. Trucks, H. B. Schlegel, G. E. Scuseria, M. A. Robb, J. R. Cheeseman, G. Scalmani, V. Barone, G. A. Petersson, H. Nakatsuji, X. Li, M. Caricato, A. V. Marenich, J. Bloino, B. G. Janesko, R. Gomperts, B. Mennucci, H. P. Hratchian, J. V. Ortiz, A. F. Izmaylov, J. L. Sonnenberg, D. Williams-Young, F. Ding, F. Lipparini, F. Egidi, J. Goings, B. Peng, A. Petrone, T. Henderson, D. Ranasinghe, V. G. Zakrzewski, J. Gao, N. Rega, G. Zheng, W. Liang, M. Hada, M. Ehara, K. Toyota, R. Fukuda, J. Hasegawa, M. Ishida, T. Nakajima, Y. Honda, O. Kitao, H. Nakai, T. Vreven, K. Throssell, J. A. Montgomery, Jr., J. E. Peralta, F. Ogliaro, M. J. Bearpark, J. J. Heyd, E. N. Brothers, K. N. Kudin, V. N. Staroverov, T. A. Keith, R. Kobayashi, J. Normand, K. Raghavachari, A. P. Rendell, J. C. Burant, S. S. Iyengar, J. Tomasi, M. Cossi, J. M. Millam, M. Klene, C. Adamo, R. Cammi, J. W. Ochterski, R. L. Martin, K. Morokuma, O. Farkas, J. B. Foresman and D. J. Fox, *Gaussian 16, Revision A.03*, Gaussian, Inc., Wallingford, CT, 2016.
39 J. Tomasi and M. Persico, *Chem. Rev.*, 1994, **94**, 2027–2094.
40 G. Henkelman, B. P. Uberuaga and H. Jónsson, *J. Chem. Phys.*, 2000, **113**, 9901.
41 Y. Luo, Z. Chen, Z. Xu and D. Tang, *New J. Chem.*, 2023, **47**, 3793–3801.
42 G. Treboux, J. Mizukami, M. Yabe and S. Nakamura, *Chem. Lett.*, 2007, **36**, 1344–1345.
43 T. Sajoto, P. I. Djurovich, A. B. Tamayo, J. Oxgaard, W. A. Goddard and M. E. Thompson, *J. Am. Chem. Soc.*, 2009, **131**, 9813–9822.